Chemical Science

ROYAL SOCIETY OF CHEMISTRY

EDGE ARTICLE

View Article Online
View Journal | View Issue

Check for updates

Cite this: *Chem. Sci.*, 2021, **12**, 3290

All publication charges for this article have been paid for by the Royal Society of Chemistry

Received 18th September 2020
Accepted 4th January 2021

DOI: 10.1039/d0sc05163b

rsc.li/chemical-science

Open Access Article. Published on 05 January 2021. Downloaded on 9/13/2025 10:43:04 PM.
This article is licensed under a Creative Commons Attribution 3.0 Unported Licence.

Cd-driven surface reconstruction and photodynamics in gold nanoclusters†

Xu Liu, ‡[a] Guo Yao,‡[b] Xinglian Cheng,‡[a] Jiayu Xu,[a] Xiao Cai,[a] Weigang Hu,[a] Wen Wu Xu, *[c] Chunfeng Zhang[b] and Yan Zhu *[a]

With atomically precise gold nanoclusters acting as a starting unit, substituting one or more gold atoms of the nanocluster with other metals has become an effective strategy to create metal synergy for improving catalytic performances and other properties. However, so far detailed insight into how to design the gold-based nanoclusters to optimize the synergy is still lacking, as atomic-level exchange between the surface-gold (or core-gold) and the incoming heteroatoms is quite challenging without changing other parts. Here we report a Cd-driven reconstruction of $Au_{44}(DMBT)_{28}$ (DMBT = 3,5-dimethylbenzenethiol), in which four $Au_2(DMBT)_3$ staples are precisely replaced by two $Au_5Cd_2(DMBT)_{12}$ staples to form $Au_{38}Cd_4(DMBT)_{30}$ with the face-centered cubic inner core retained. With the dual modifications of the surface and electronic structure, the $Au_{38}Cd_4(DMBT)_{30}$ nanocluster exhibits distinct excitonic behaviors and superior photocatalytic performances compared to the parent $Au_{44}(DMBT)_{28}$ nanocluster.

Introduction

Metal synergy is of paramount importance as the rationale to modulate the intrinsic properties of metal nanoparticles.[1,2] However, the precise synergistic interaction in an intermetallic nanoparticle has so far been elusive, due to the challenges in determining the atomic-level arrangement of the metal heteroatoms in the nanoparticle. Atomically precise metal nanoparticles (often called nanoclusters) lead to unprecedented opportunities in signalling clear directions to exploit the cooperativity between the two metal elements within a single nanocluster.[3] Thiolate-protected gold nanoclusters, $Au_n(SR)_m$, where n is the number of gold atoms and m is the number of thiolate ligands, SR, have gained momentum over the past few years as an exciting area and have opened up new horizons in precise tailoring of the composition and structure to control the physicochemical properties.[4–12] The $Au_n(SR)_m$ nanoclusters are typically configured with an inner gold core (or kernel) and various surface motifs, in which the motifs containing both gold and thiolate resemble staples. Both the gold core and the surface motifs can contribute to the physicochemical properties such as the optical and electronic properties, as well as catalysis.[13–18] It has been recognized that substituting one or more gold atoms in either the core or the motifs with other metals can tune the overall performances of the parent nanoclusters.[19–26] Therefore, it has become possible to access the previously inaccessible metal synergy in the bimetallic nanoclusters with atomic-precision.

Among the gold-based bimetal nanoclusters, cadmium-containing bimetal clusters provide synergistic strategies to adjust the electronic structures and further modulate the physicochemical properties in the clusters, since Cd has one more valence electron than Au.[21,26,27] Cd introduction usually causes surface reconstruction of gold nanoclusters. For example, $Au_{19}Cd_2(SR)_{16}$ was obtained through the substitution of two neighboring surface Au atoms with one Cd with the cuboctahedral Au_{13} unchanged.[26] $Au_{19}Cd_3(SR)_{18}$ was formed by retaining the icosahedral Au_{13} core but only changing the surface of $Au_{25}(SR)_{18}$.[27] However, the surface reconstruction strategy remains challenging and no examples of bimetal clusters formed without breaking the face-centered cubic (fcc) core of the parent gold clusters have been documented, which might thus impede gaining a higher understanding of how to tailor the surface structure of gold-based nanoclusters and accordingly optimize their synergy.

Herein, we report our success in synthesizing a $Au_{38}Cd_4(DMBT)_{30}$ (DMBT = 3,5-dimethylbenzenethiol) nanocluster that is obtained from the surface reconstruction of $Au_{44}(DMBT)_{28}$ induced by Cd^{2+}. The fcc Au_{26} kernel originating from $Au_{44}(DMBT)_{28}$, which is assembled from Au_4 tetrahedra, is retained in the $Au_{38}Cd_4(DMBT)_{30}$. The $Au_{38}Cd_4(DMBT)_{30}$ nanocluster exhibits distinctly different excited-state dynamics from $Au_{44}(DMBT)_{28}$. More interestingly, the $Au_{38}Cd_4(DMBT)_{30}$ nanocluster

[a]*School of Chemistry and Chemical Engineering, Nanjing University, Nanjing 210093, China. E-mail: zhuyan@nju.edu.cn*

[b]*School of Physics, Nanjing University, Nanjing 210093, China*

[c]*School of Physical Science and Technology, Ningbo University, Ningbo 315211, China. E-mail: xuwenwu@nbu.edu.cn*

† Electronic supplementary information (ESI) available. CCDC 2022214 and 2022215. For ESI and crystallographic data in CIF or other electronic format see DOI: 10.1039/d0sc05163b

‡ These authors contributed equally to this work.

© 2021 The Author(s). Published by the Royal Society of Chemistry

Open Access Article. Published on 05 January 2021. Downloaded on 9/13/2025 10:43:04 PM.
This article is licensed under a Creative Commons Attribution 3.0 Unported Licence.

as a photocatalyst shows better visible light-driven catalytic activity than the parent $Au_{44}(DMBT)_{28}$ catalyst.

Results and discussion

X-ray crystallography analysis shows that the parent $Au_{44}(DMBT)_{28}$ nanocluster is composed of an Au_{26} kernel, six $Au_2(SR)_3$ and two $Au(SR)_2$ staples (Fig. 1a, c and Table S1†). The formula of $Au_{44}(DMBT)_{28}$ is further confirmed by electrospray ionization mass spectroscopy (ESI-MS, Fig. S1a†). The structural framework of $Au_{44}(DMBT)_{28}$ is identical to that of the reported $Au_{44}(TBBT)_{28}$ (TBBT = 4-*tert*-butylbenzenethiol) (Fig. S2†),[28] both of which can be assembled into the layered structures (Fig. S3–S5†). Notably, a significant difference is observed in the layer's interior, where all the molecules of $Au_{44}(TBBT)_{28}$ in the layer (marked with the same color, Fig. S3†) are packed along the same direction, while $Au_{44}(DMBT)_{28}$ molecules are arranged in different directions (Fig. S5†). Such a difference may be ascribed to the different steric hindrance between TBBT and DMBT. The UV-vis-NIR spectra of the two $Au_{44}(SR)_{28}$ nanoclusters show only small deviations. As shown in Fig. S6,† the prominent peak at 380 nm for $Au_{44}(TBBT)_{28}$ is slightly red-shifted to 388 nm for $Au_{44}(DMBT)_{28}$, and the broad peaks at 650 and 725 nm become apparent when TBBT is replaced by DMBT.

With $Au_{44}(DMBT)_{28}$ as a starting unit, a Cd-doped nanocluster was further synthesized *via* an ion-exchange strategy. From ESI-MS data (Fig. S1b†), the prominent peak at 6025.43 *m*/*z* with a +2 charge is assigned to $Au_{38}Cd_4(DMBT)_{30}$ (theoretical value: 6025.48 *m*/*z*), which is further confirmed by the excellent match between experimental and calculated isotopic patterns (inset of Fig. S1b†). Single crystallography analysis reveals that $Au_{38}Cd_4(DMBT)_{30}$ contains a 26-Au-atom kernel, two $Au_5Cd_2(SR)_{12}$ staples, two $Au(SR)_2$ staples and two bridging SR ligands,

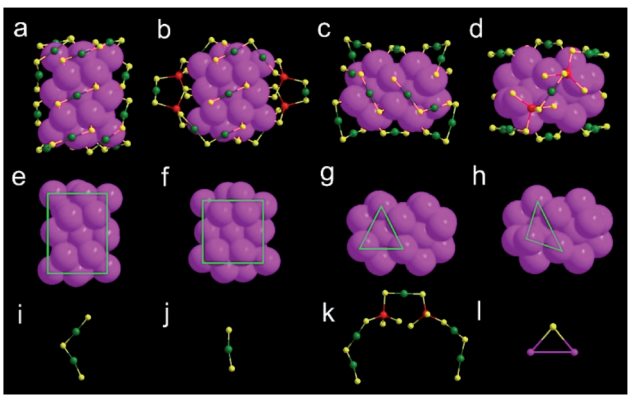

Fig. 1 Structural analysis of $Au_{44}(DMBT)_{28}$ and $Au_{38}Cd_4(DMBT)_{30}$ nanoclusters in the space-filling mode. Total structures of (a) $Au_{44}(DMBT)_{28}$ and (b) $Au_{38}Cd_4(DMBT)_{30}$ viewed from the front. Total structures of (c) $Au_{44}(DMBT)_{28}$ and (d) $Au_{38}Cd_4(DMBT)_{30}$ viewed from the side. Au_{26} kernels of (e) $Au_{44}(DMBT)_{28}$ and (f) $Au_{38}Cd_4(DMBT)_{30}$ viewed from the front. Au_{26} kernels of (g) $Au_{44}(DMBT)_{28}$ and (h) $Au_{38}Cd_4(DMBT)_{30}$ viewed from the side. Note that green frames show kernel distortions. Various motifs of the two nanoclusters: (i) $Au_2(SR)_3$; (j) $Au(SR)_2$; (k) $Au_5Cd_2(SR)_{12}$; (l) SR; color codes: magenta/green = Au, yellow = S, red = Cd. C and H atoms are omitted for clarity.

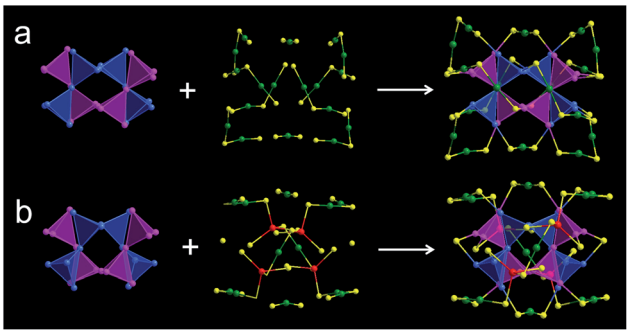

Fig. 2 Structural anatomy of (a) $Au_{44}(DMBT)_{28}$ and (b) $Au_{38}Cd_4(DMBT)_{30}$ with the fcc Au_{26} kernels assembled from Au_4 building blocks. Color codes: blue/magenta/green = Au, yellow = S, red = Cd. C and H atoms are omitted for clarity.

as shown in Fig. 1b, d, and Table S2.† Note that the retained kernel of $Au_{38}Cd_4(DMBT)_{30}$ experiences a slight distortion from "slender" to "stocky" in comparison with that of the parent $Au_{44}(DMBT)_{28}$ (Fig. 1e–h). Further analysis shows that the Au_{26} kernel in $Au_{38}Cd_4(DMBT)_{30}$ can be viewed as the assembly of tetrahedral Au_4 units in a double-helical mode, as well as that in $Au_{44}(DMBT)_{28}$ (Fig. 2). Furthermore, the two nanoclusters have almost identical distances between neighboring Au_4 units, which is clearly manifested in the similar Au–Au bond lengths according to the different positions of the Au atoms (Fig. S7†). Therefore, $Au_{38}Cd_4(DMBT)_{30}$ can be viewed as the gentle surface reconstruction without breaking the double-helical Au_{26} kernel based on the parent $Au_{44}(DMBT)_{28}$. In addition, $Au_{38}Cd_4(DMBT)_{30}$ is also patterned along different directions in the layer structure (Fig. S8†).

To gain an in-depth insight into the Cd-induced surface reconstruction mechanism, density functional theory (DFT) calculations were performed. Starting from the $Au_{44}(SR)_{28}$ cluster, as presented in Fig. S9,† four $Au_2(SR)_3^-$ protecting motifs of $Au_{44}(SR)_{28}$ are substituted by six $Cd(SR)_2$, resulting in the formation of an unstable intermediate, $Au_{36}Cd_6(SR)_{28}^{4+}$, due to the very high substitution energy (24.80 eV, step 1). After this, a surface isomerization of $Au_{36}Cd_6(SR)_{28}^{4+}$ is considered *via* the reorganization of the motifs (step 2). In this step, the Cd atom in $Cd(SR)_2$ binds with a neighboring S atom in the SR $[Au(SR)]_2^-$ motif, which is accompanied by the breaking of a Au–S bond and the formation of a naked Au atom. The S atom in $Cd(SR)_2$ binds with this naked Au atom to form a new Au–S bond. Therefore, the structure in which the three-coordinated μ_3-Cd atoms bind with two SR^- and one $Au(SR)_2^-$ can be obtained during the structural isomerization of $Au_{36}Cd_6(SR)_{28}^{4+}$. In addition, the $Au_{36}Cd_6(SR)_{28}^{4+}$ becomes more stable after isomerization *via* lowering the energy by 3.37 eV. Then, two S atoms of the $SR[Au(SR)]^-$ motif further bind with two μ_3-Cd atoms to form two four-coordinated μ_4-Cd atoms, resulting in the formation of a more stable intermediate structure, $Au_{38}Cd_6(SR)_{32}^{2+}$, with a formation energy of −18.64 eV (step 3). In step 4, the SR^- motif binds with the Cd atom of $Cd(SR)_2$ to form $Cd(SR)_3^-$, in which the $Cd(SR)_2$ is quickly separated from $Cd(SR)_3^-$ leaving a bridging SR^- motif on the surface of the Au

Open Access Article. Published on 05 January 2021. Downloaded on 9/13/2025 10:43:04 PM.
This article is licensed under a Creative Commons Attribution 3.0 Unported Licence.

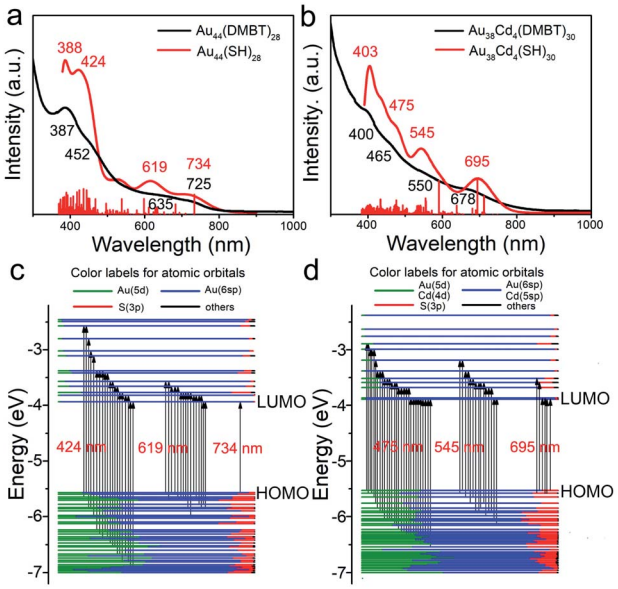

Fig. 3 Experimental and calculated UV-vis-NIR spectra of (a) $Au_{44}(DMBT)_{28}$ and (b) $Au_{38}Cd_4(DMBT)_{30}$ nanoclusters and molecular orbital (MO) energy level diagrams for (c) $Au_{44}(SR)_{28}$ and (d) $Au_{38}Cd_4(SR)_{30}$. The convolution factor of the convoluted spectra is 0.1 eV.

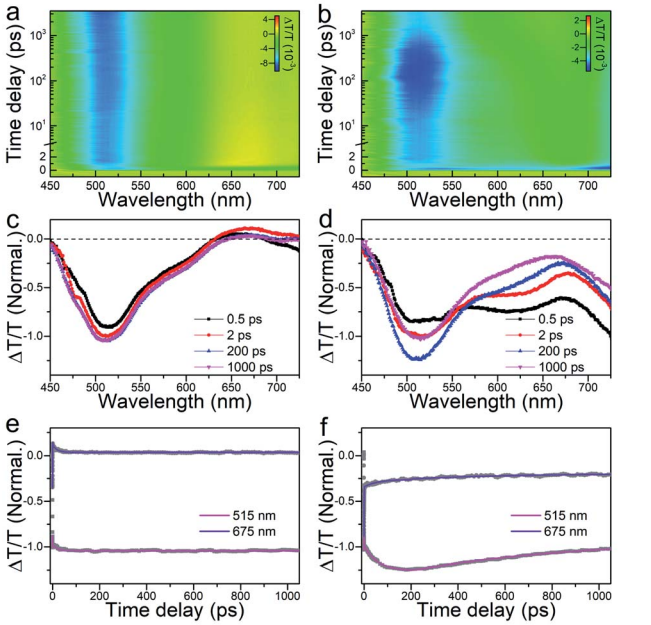

Fig. 4 Femtosecond-resolved TA spectra of (a) $Au_{44}(DMBT)_{28}$ and (b) $Au_{38}Cd_4(DMBT)_{30}$ pumped at 400 nm. Time evolution of femtosecond-resolved TA spectra of (c) $Au_{44}(DMBT)_{28}$ and (d) $Au_{38}Cd_4(DMBT)_{30}$. Kinetic traces at selected wavelengths of (e) $Au_{44}(DMBT)_{28}$ and (f) $Au_{38}Cd_4(DMBT)_{30}$. The data are plotted in a scale normalized to the amplitude of the signal probed at 515 nm at a delay of 2 ps. The gray dots in (e) and (f) are the original data, while the corresponding multi-exponential fits are plotted as colored lines.

core. Finally, the stable $Au_{38}Cd_4(SR)_{30}$ is formed with a formation energy of −12.50 eV. The proposed conversion process from $Au_{44}(SR)_{28}$ to $Au_{38}Cd_4(SR)_{30}$ includes two key steps: (i) the substitution of $SR[Au(SR)]_2^-$ by $Cd(SR)_2$ and (ii) the structural isomerization of surface ligands.

To investigate the electronic structure changes induced by Cd-atom surface modification, the optical adsorption spectra of the $Au_{44}(DMBT)_{28}$ and $Au_{38}Cd_4(DMBT)_{30}$ nanoclusters were measured. The absorption peaks of $Au_{38}Cd_4(DMBT)_{30}$ are mainly centered at 400, 465, 550 and 678 nm (Fig. 3b), which differ from those observed in the parent nanocluster (387, 452, 635 and 725 nm; Fig. 3a). These optical features can be well reproduced by theoretical calculations (Fig. 3a, b and S10†). The Kohn–Sham (KS) molecular orbital (MO) energy levels and atomic orbital components in each KS MO of $Au_{44}(SR)_{28}$ and $Au_{38}Cd_4(SR)_{30}$ suggest that the absorption peaks mainly involve the Au(sp) → Au(sp) transitions (Fig. 3c and d). In particular, for $Au_{44}(SR)_{28}$, the first absorption peak centered at 734 nm originates from the highest occupied molecular orbital → the lowest unoccupied molecular orbital (HOMO → LUMO) transition, while for $Au_{38}Cd_4(SR)_{30}$, the first absorption peak centered at 695 nm originates from the HOMO → LUMO, HOMO → LUMO+1, HOMO → LUMO+4, HOMO−1 → LUMO, HOMO−1 → LUMO+1, and HOMO−1 → LUMO+5 transitions. The more complex orbital transitions in $Au_{38}Cd_4(SR)_{30}$ than in $Au_{44}(SR)_{28}$ can be attributed to the dopant Cd. This behaviour can also be observed for other absorption peaks.

Moreover, femtosecond and nanosecond carrier dynamics of the two nanoclusters were measured *via* time-resolved transient absorption (TA) spectroscopy to decipher their potential energy-related applications. The femtosecond-resolved TA spectra of the $Au_{44}(DMBT)_{28}$ and $Au_{38}Cd_4(DMBT)_{30}$ nanoclusters are provided in Fig. 4a and b. Similarly, both $Au_{44}(DMBT)_{28}$ and $Au_{38}Cd_4(DMBT)_{30}$ nanoclusters showed broad excited state absorption (ESA) signals overlapped with ground state bleaching (GSB) peaks near 675 nm. We selectively extracted the TA spectra at different delay times, combined with the dynamic traces probed at 515 and 675 nm to study the transient evolution and the relaxation dynamics (Fig. 4c–f). A 0.6 ps process at the early stage, which is attributed to the ultrafast internal conversion from higher excited states to lower excited states,[29] was observed in the two nanoclusters (Fig. S11 and Table S3†). It is worth noting that the major divergence between the two nanocluster systems emerged after a delay of 2 ps. For $Au_{44}(DMBT)_{28}$, the TA spectra remained nearly unchanged after 2 ps (Fig. 4c), which is consistent with the flat decay kinetic traces shown in Fig. 4e. A 19 ps process obtained by exponential fitting was ascribed to the structural relaxation caused by conformational changes after pumping.[29–31] For $Au_{38}Cd_4(DMBT)_{30}$, interestingly, an obvious spectral transformation was observed and the lifetime of this component was determined to be 57 ps (Table S3†), which differs from the 19 ps structural relaxation observed in $Au_{44}(DMBT)_{28}$ and might be related to the charge transfer states between the ligand and the metal core of $Au_{38}Cd_4(DMBT)_{30}$,[32–35] which can be manifested by the overall Hirshfeld charge of the Au_{26} core in $Au_{38}Cd_4(SH)_{30}$ (0.46) and in $Au_{44}(SH)_{28}$ (0.56). Of note, deduced from nanosecond-resolved TA analysis, as shown in Fig. S12,† the $Au_{38}Cd_4(DMBT)_{30}$ nanocluster exhibits a faster carrier recombination process with

© 2021 The Author(s). Published by the Royal Society of Chemistry

Open Access Article. Published on 05 January 2021. Downloaded on 9/13/2025 10:43:04 PM.
This article is licensed under a Creative Commons Attribution 3.0 Unported Licence.

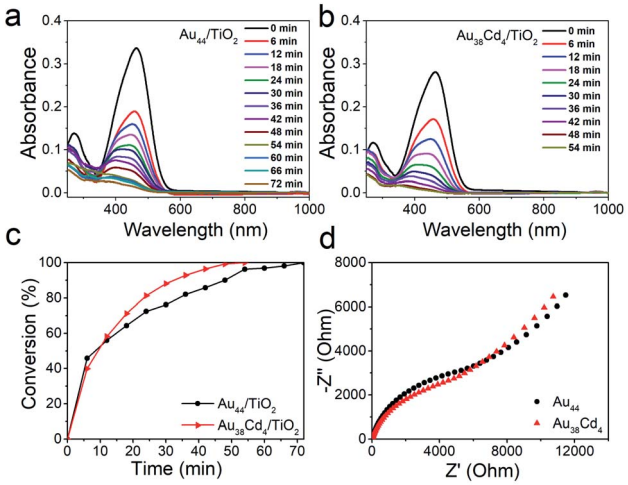

Fig. 5 Photocatalytic degradation of methyl orange over (a) $Au_{44}(DMBT)_{28}/TiO_2$ and (b) $Au_{38}Cd_4(DMBT)_{30}/TiO_2$ under visible light illumination. (c) Visible light-driven degradation of methyl orange by $Au_{38}Cd_4(DMBT)_{30}/TiO_2$ and $Au_{44}(DMBT)_{28}/TiO_2$ catalysts. Reaction conditions: 40 mg catalyst, 20 mL H_2O, 0.1 mL (1 g L^{-1}) methyl orange. (d) Electrochemical impedance spectra of the $Au_{38}Cd_4(DMBT)_{30}$ and $Au_{44}(DMBT)_{28}$ nanoclusters.

a lifetime of 253 ns than the $Au_{44}(DMBT)_{28}$ nanocluster (389 ns lifetime), readily supporting the putative synergy in the $Au_{38}Cd_4(DMBT)_{30}$ nanocluster being invoked in underpinning the excited-state dynamics.

The distinguishable electronic and optical properties of the two nanoclusters would apparently impact their catalytic properties. Thus, visible light-driven degradation of methyl orange was selected to explore the photocatalysis of the two nanoclusters. From Fig. 5a and b, within 50 min, methyl orange can be completely degraded on the $Au_{38}Cd_4(DMBT)_{30}$ catalyst under visible light illumination, while on the $Au_{44}(DMBT)_{28}$ catalyst it was completed in 70 min. The plots of methyl orange degradation on the catalysts *versus* reaction time further indicate the better photocatalytic performance of the $Au_{38}Cd_4(DMBT)_{30}$ catalyst (Fig. 5c). Electrochemical impedance spectroscopy was performed to investigate the interfacial transfer of electrons. In Fig. 5d, the semicircular diameter of $Au_{38}Cd_4(DMBT)_{30}$ was smaller than that of $Au_{44}(DMBT)_{28}$, which implies faster electron-transfer in the $Au_{38}Cd_4(DMBT)_{30}$ system. The photocatalysis difference in the two cluster catalysts is suggested to arise from their different equilibria established between the carrier recombination and the electron transfer influenced by metal synergy.

Conclusions

In summary, we have developed a Cd-driven surface reconstruction strategy for synthesizing a new $Au_{38}Cd_4(DMBT)_{30}$ bimetallic nanocluster with the fcc Au_{26} core retained from the parent $Au_{44}(DMBT)_{28}$ nanocluster. The two nanoclusters that exhibit elegant patterns of Au_4 tetrahedra show distinct differences in the electronic structures, optical properties, and photocatalytic performances. Beyond the Cd-mediated surface reconstruction case, we anticipate that this heteroatom-doping mechanism will find applications in using gold and other metals in a series of challenging gold-based nanocluster formations and tuning of their intrinsic properties.

Conflicts of interest

There are no conflicts to declare.

Acknowledgements

We acknowledge the financial support from the National Natural Science Foundation of China (21773109, 91845104 and 11974195), China Postdoctoral Science Foundation (2019M650106, 2020T130286), and Programs for high-level entrepreneurial and innovative talents introduction of Jiangsu Province (individual and group program).

Notes and references

1 A. C. Deacy, A. F. R. Kilpatrick, A. Regoutz and C. K. Williams, *Nat. Chem.*, 2020, **12**, 372–380.
2 N. Zou, X. Zhou, G. Chen, N. M. Andoy, W. Jung, G. Liu and P. Chen, *Nat. Chem.*, 2018, **10**, 607–614.
3 Y. Sun, W. Pei, M. Xie, S. Xu, S. Zhou, J. Zhao, K. Xiao and Y. Zhu, *Chem. Sci.*, 2020, **11**, 2240–2247.
4 P. D. Jadzinsky, G. Calero, C. J. Ackerson, D. A. Bushnell and R. D. Kornberg, *Science*, 2007, **318**, 430–433.
5 C. Zeng, Y. Chen, K. Kirschbaum, K. J. Lambright and R. Jin, *Science*, 2016, **354**, 1580–1584.
6 J. Yan, B. K. Teo and N. Zheng, *Acc. Chem. Res.*, 2018, **51**, 3084–3093.
7 Y. Negishi, K. Nobusada and T. Tsukuda, *J. Am. Chem. Soc.*, 2005, **127**, 5261–5270.
8 Y. Song, F. Fu, J. Zhang, J. Chai, X. Kang, P. Li, S. Li, H. Zhou and M. Zhu, *Angew. Chem., Int. Ed.*, 2015, **127**, 8550–8554.
9 Z. Wu, Y. Du, J. Liu, Q. Yao, T. Chen, Y. Cao, H. Zhang and J. Xie, *Angew. Chem., Int. Ed.*, 2019, **58**, 8139–8144.
10 A. Baksi, P. Chakraborty, S. Bhat, G. Natarajan and T. Pradeep, *Chem. Commun.*, 2016, **52**, 8397–8400.
11 C. Zeng, Y. Chen, C. Liu, K. Nobusada, N. L. Rosi and R. Jin, *Sci. Adv.*, 2015, **1**, e1500425.
12 L. Shi, L. Zhu, J. Guo, L. Zhang, Y. Shi, Y. Zhang, K. Hou, Y. Zheng, Y. Zhu, J. Lv, S. Liu and Z. Tang, *Angew. Chem., Int. Ed.*, 2017, **56**, 15397–15401.
13 R. Jin, C. Zeng, M. Zhou and Y. Chen, *Chem. Rev.*, 2016, **116**, 10346–10413.
14 M. A. Tofanelli, K. Salorinne, T. W. Ni, S. Malola, B. Newell, B. Phillips, H. Häkkinen and C. J. Ackerson, *Chem. Sci.*, 2016, **7**, 1882–1890.
15 X. Cai, G. Saranya, K. Shen, M. Chen, R. Si, W. Ding and Y. Zhu, *Angew. Chem., Int. Ed.*, 2019, **58**, 9964–9968.
16 K. Kwak, W. Choi, Q. Tang, M. Kim, Y. Lee, D. E. Jiang and D. Lee, *Nat. Commun.*, 2017, **8**, 14723.
17 S. Li, H. Chen, X. Liu, H. Liu, J. Ma and Y. Zhu, *Chem. Sci.*, 2020, **11**, 8000–8004.

© 2021 The Author(s). Published by the Royal Society of Chemistry

Open Access Article. Published on 05 January 2021. Downloaded on 9/13/2025 10:43:04 PM.
This article is licensed under a Creative Commons Attribution 3.0 Unported Licence.

18 X. Wan, J. Wang, Z. Nan and Q. Wang, *Sci. Adv.*, 2017, **3**, e1701823.
19 S. Takano, S. Hasegawa, M. Suyama and T. Tsukuda, *Acc. Chem. Res.*, 2018, **51**, 3074–3083.
20 Q. Li, T. Luo, M. G. Taylor, S. Wang, X. Zhu, Y. Song, G. Mpourmpakis, N. L. Rosi and R. Jin, *Sci. Adv.*, 2017, **3**, e1603193.
21 S. Zhuang, D. Chen, L. Liao, Y. Zhao, N. Xia, W. Zhang, C. Wang, J. Yang and Z. Wu, *Angew. Chem., Int. Ed.*, 2020, **59**, 3073–3077.
22 W. Fei, S. Antonello, T. Dainese, A. Dolmella, M. Lahtinen, K. Rissanen, A. Venzo and F. Maran, *J. Am. Chem. Soc.*, 2019, **141**, 16033–16045.
23 H. Qian, D. E. Jiang, G. Li, C. Gayathri, A. Das, R. R. Gil and R. Jin, *J. Am. Chem. Soc.*, 2012, **134**, 16159–16162.
24 X. Cai, W. Hu, S. Xu, D. Yang, M. Chen, M. Shu, R. Si, W. Ding and Y. Zhu, *J. Am. Chem. Soc.*, 2020, **142**, 4141–4153.
25 M. Suyama, S. Takano, T. Nakamura and T. Tsukuda, *J. Am. Chem. Soc.*, 2019, **141**, 14048–14051.
26 Q. Li, K. L. Lambright, M. G. Taylor, K. Kirschbaum, T. Luo, J. Zhao, G. Mpourmpakis, S. Mokashi-Punekar, N. L. Rosi and R. Jin, *J. Am. Chem. Soc.*, 2017, **139**, 17779–17782.
27 C. Yao, C. Xu, I. Park, M. Zhao, Z. Zhu, J. Li, X. Hai, H. Fang, Y. Zhang, G. Macam, J. Teng, L. Li, Q. Xu, F. Chuang, J. Lu, C. Su, J. Li and J. Lu, *Angew. Chem., Int. Ed.*, 2020, **59**, 8270–8276.
28 C. Zeng, Y. Chen, K. Iida, K. Nobusada, K. Kirschbaum, K. J. Lambright and R. Jin, *J. Am. Chem. Soc.*, 2016, **138**, 3950–3953.
29 M. Zhou, C. Zeng, M. Y. Sfeir, M. Cotlet, K. Iida, K. Nobusada and R. Jin, *J. Phys. Chem. Lett.*, 2017, **8**, 4023–4030.
30 M. Zhou, S. Tian, C. Zeng, M. Y. Sfeir, Z. Wu and R. Jin, *J. Phys. Chem. C*, 2017, **121**, 10686–10693.
31 M. Zhou, T. Higaki, Y. Li, C. Zeng, Q. Li, M. Y. Sfeir and R. Jin, *J. Am. Chem. Soc.*, 2019, **141**, 19754–19764.
32 Z. Wu and R. Jin, *Nano Lett.*, 2010, **10**, 2568–2573.
33 S. A. Miller, C. A. Fields-Zinna, R. W. Murray and A. M. Moran, *J. Phys. Chem. Lett.*, 2010, **1**, 1383–1387.
34 K. L. D. M. Weerawardene and C. M. Aikens, *J. Am. Chem. Soc.*, 2016, **138**, 11202–11210.
35 X. Kang, S. Wang, Y. Song, S. Jin, G. Sun, H. Yu and M. Zhu, *Angew. Chem., Int. Ed.*, 2016, **55**, 3611–3614.

© 2021 The Author(s). Published by the Royal Society of Chemistry